Enhanced Electrochemical Hydrogenation of Benzaldehyde to Benzyl Alcohol on Pd@Ni-MOF by Modifying the Adsorption Configuration

Li Gong[a,b], Chaoyue Zhang[a,c]*, Junshan Li [d], Guillem Montaña-Mora[a,b], Marc Botifoll[e], Jordi Arbiol[e], Jinyuan Zhou[c], Tanja Kallio[g], Paulina R. Martínez-Alanis[a]*, Andreu Cabot[a,f]*

[a] Catalonia Institute for Energy Research – IREC Sant Adrià de Besòs, Barcelona 08930, Spain

[b] University of Barcelona, Barcelona 08028, Spain.

[c] Key Laboratory for Magnetism and Magnetic Materials of the Ministry of Education & School of Physical Science & Technology, Lanzhou University, Lanzhou, 730000, China.

[d] Institute for Advanced Study, Chengdu University, Chengdu, 610106, China

[e] Catalan Institute of Nanoscience and Nanotechnology (ICN2), CSIC and BIST, Campus UAB, Bellaterra, 08193, Barcelona, Spain.

[f] Catalan Institution for Research and Advanced Studies – ICREA Pg. Lluís Companys 23, 08010, Barcelona, Spain

[g] Department of Chemistry and Materials Science, Aalto University School of Chemical Engineering, P.O. Box 16100, FI-00076 Aalto, Finland.

---

*Corresponding authors.
E-mail addresses: chzhang@irec.cat (C.Y. Zhang); pmartinez@irec.cat (P. R. Martínez-Alanis), acabot@irec.cat (Andreu Cabot)

Abstract: Electrocatalytic hydrogenation (ECH) approaches under ambient temperature and pressure offer significant potential advantages over thermal hydrogenation processes. However, to take advantage of such ECH routes, highly active and efficient hydrogenation electrocatalysts need to be developed. Herein, the engineering of Pd nanoparticles supported on a nickel metal–organic framework (MOF), Ni-MOF-74, is demonstrated and their activity towards the ECH of benzaldehyde (BZH) in an aqueous electrolyte is explored. An outstanding ECH rate up to 283 μmol cm^{-2} h^{-1} with a Faradic efficiency (FE) of 76% is reached. Besides, higher FEs of up to 96% are achieved using a step-function voltage. Materials studio and density functional theory calculations show these outstanding performances to be associated with the Ni-MOF support that promotes H-bond formation, facilitates water desorption, and induces a favorable tilted BZH adsorption. In this configuration, BZH is bonded by the carbonyl group rather than through the aromatic ring, thus reducing the energy barriers of the elemental reaction steps and increasing the overall reaction efficiency.

Keywords: Electrochemical hydrogenation; metal-organic-framework; palladium; benzaldehyde; benzyl alcohol

1. Introduction

Biomass is a convenient precursor for the carbon-negative production of chemical commodities and fuels. Thus, the development of valorization strategies for the efficient and cost-effective conversion of biomass feedstocks has become a research priority.[1-3] Biomass valorization schemes generally involve several steps, including feedstock deconstruction, conversion of solid biomass into a liquid bio-oil for convenient transportation and post-processing, and multiple deoxygenation and hydrogenation reactions to upgrade the oxygen-rich and hydrogen-poor biomass derivate into higher value chemicals, particularly fuels. Usually, several thermocatalytic steps and highly pressurized hydrogen are required in this process, which limits cost-effectiveness, especially within a small-scale distributed scenario that reflects and adapts to the distributed nature of biomass.[3]

Alternative electrocatalytic approaches, taking advantage of protons within the electrolyte instead of highly pressurized hydrogen, are particularly advantageous in terms of energy efficiency, mild reaction conditions including relatively low temperatures ≤ 80 ºC, cost, and feasibility of combining with clean electricity provided by renewable energy sources such as wind and photovoltaics.[4-9] These advantages also make electrocatalytic hydrogenation (ECH) schemes suitable for distributed processing.[3]

Benzyl alcohol (BA) is a chemical commodity used as a solvent in the fields of printing and coatings, as a desiccant of polymers such as nylon, as a precursor for the preparation of esters, and as an additive in the fragrance industry.[10] The conventional industrial methods for producing BA is the toluene chlorination to benzyne chloride and subsequent hydrolysis.[11] This route produces chlorine residues that are harmful to the environment. Thus, the production of BA from the selective catalytic reduction of benzaldehyde (BZH), which can be obtained from lignin depolymerization,[12] is considered a convenient green alternative.

Despite the benefits of ECH schemes over conventional catalytic hydrogenation approaches, the ECH of BZH to BA has been rarely explored. Among the transition metal electrocatalysts tested for this reaction,[13] Pd is considered the most active metal because it has an optimum interaction strength with BZH, with a computed binding of −3.16 eV.[14]

Beyond the active phase, the support plays a fundamental role in ECH reactions. Large surface area supports are needed to enable a high dispersion of the active phase. In this direction, the large surface area and tunable structure of metal-organic frameworks (MOFs) offer an ideal architecture to support catalytic active centers. Besides, the metal nodes and aromatic linkers of MOFs can modify electronic interactions through synergistic interaction between the different elements and π-π forces,[15-17] thereby potentially enhancing the stability and activity of the active centers. Besides dispersing the active phase, supports play a strong role in binding the reactant molecule or its intermediates. In ECH processes, the simultaneous adsorption of the proton and the organic substrate on the electrically connected cathode surface is fundamental.[18-20] Thus, beyond selecting a proper active phase and having it highly dispersed on a high surface area support, the support composition, transport properties, and surface chemistry are fundamental parameters to be optimized to maximize the catalyst performance.[3] As an example, Zou’s group reported a UIO-66 MOF modified with terminal sulfonic groups that provided stronger Lewis acidic-basic and Brønsted acidic sites that contribute to the ECH of furfural to furfuryl alcohol.[21] Besides, Johannes’ group proved acid functionalization of carbon supports promotes the ECH of BZH to BA.[22]

Herein, we propose a high-performance electrocatalyst for the BZH to BA hydrogenation reaction based on Pd nanoparticles supported on an oxygen-rich Ni-MOF (Scheme 1). The system is studied both experimentally and using theoretical calculations. We particularly analyze the role of the support on the excellent performance obtained, affecting the adsorption/desorption of hydrogen, water, and BZH, and promoting its reaction.

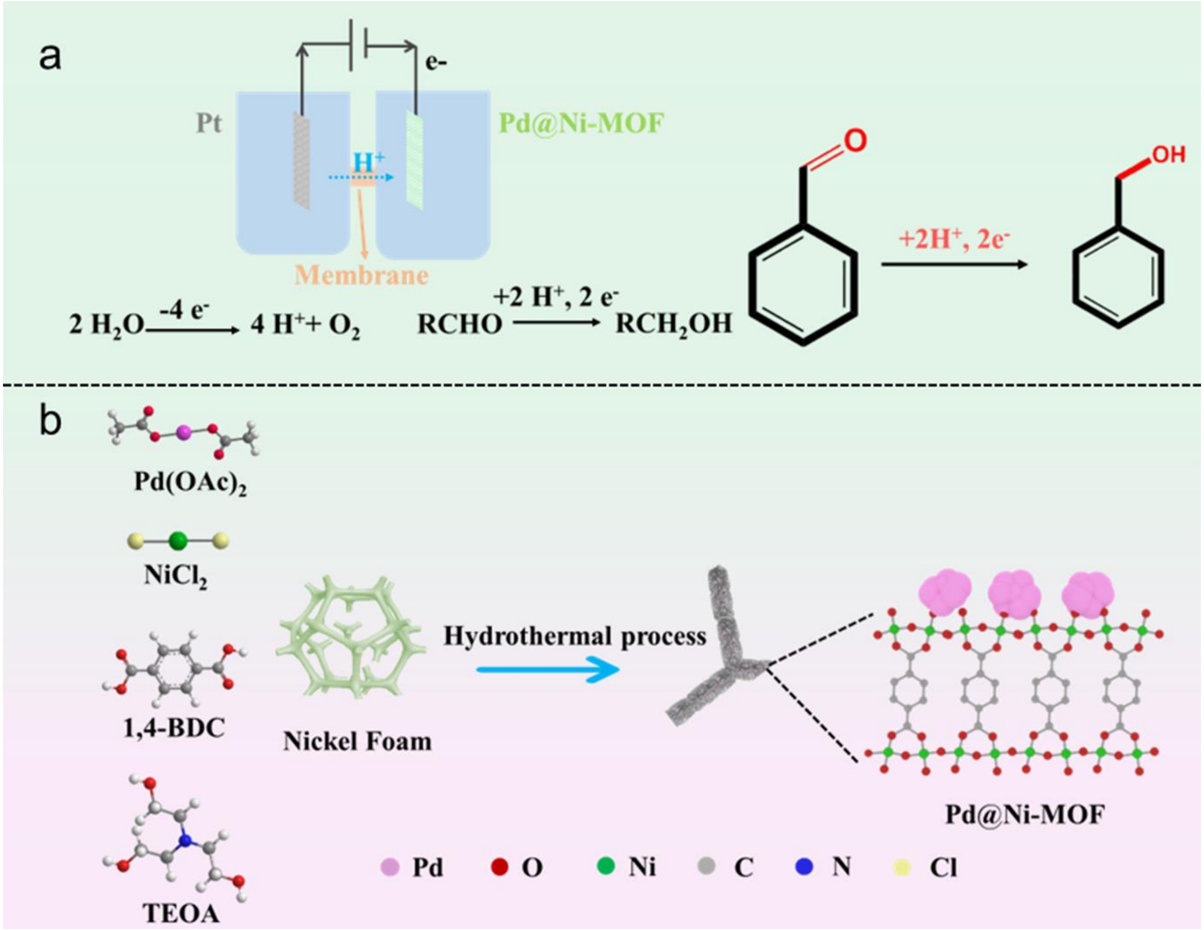

Scheme 1. (a) Illustration of the ECH of BZH to BA; (b) Scheme of the preparation process of the electrocatalyst Pd@Ni-MOF. Hydrogen atoms (white) were deleted for clarity in the supramolecular structure.

2. Experimental sections

2.1 Materials. All the chemicals were used as purchased, without further purification. Palladium(II) acetate ($Pd(OAc)_2$ 98%, Sigma Aldrich), terephthalic acid (BDC, 98%, Sigma Aldrich 98%, Sigma Aldrich), nickel(Ⅱ) chloride hexahydrates ($NiCl_2 \cdot 6H_2O$, 99.9%, Sigma

Aldrich), N,N-dimethylformamide (DMF, ⩾99.8%, Sigma Aldrich), triethanolamine (TEOA, 97%, Thermo Scientific™), ethanol (CH_3CH_2OH , 96%, Letslab), benzaldehyde (C_7H_6O, 98%, Sigma Aldrich) acetone ($(CH_3)_2CO$, Letslab), hydrochloric acid (HCl, 37%, Thermo Scientific™), and nickel foam (NF, 99.9%, Kejing).

2.2 Synthesis of Pd@Ni-MOF. 1 mmol $NiCl_2 \cdot 6 H_2O$, 1 mmol BDC, 0.2 mmol $Pd(Oac)_2$, and 1 mmol TEOA were dissolved in 22 mL of a mixture solution of DMF and milli-Q (MQ) water (20:2). After continuously stirring for 30 min, the solution was transferred into a 30 mL Teflon-lined autoclave and a piece of NF (3x2 cm^2), previously cleaned with 3 M HCl for 10 min and washed 3 times with MQ water, was placed into the solution leaning against the autoclave wall. The autoclave was sealed and heated at 120 °C for 12 h. After cooling to room temperature, the sample was thoroughly washed with DMF, MQ water, and ethanol and then dried at 60 °C overnight (mass loading: 1.2 mg cm^{-2}). This sample was named Pd@Ni-MOF. Besides, reference samples containing no TEOA (TEOA-free Pd@Ni-MOF), no Pd (Ni-MOF), and no TEOA and no Pd (TEOA-free Ni-MOF) were also produced. An additional reference material electrode was produced by loading a commercial 20% Pd supported on active carbon on NF (20% Pd@C).

2.3 Materials Characterization. The morphology of the samples (supported on the NF) was characterized by scanning electron microscopy (SEM) analysis on a Zeiss Auriga microscope (Carl Zeiss, Jena, Germany) with an energy-dispersive X-ray spectroscopy (EDX) detector at 15 kV to analyze composition. Transmission electron microscopy (TEM) analysis was carried out on unsupported samples (sonicated from NF) using a ZEISS LIBRA 120, operating at 120 kV. Scanning TEM (STEM) and high-resolution TEM (HRTEM) were carried out under a 200 keV Tecnai F20 field emission microscope. Electron energy loss spectroscopy (EELS) and high-angle annular dark-field (HAADF) STEM were carried out using a Gatan Quantum image filter embedded in the F20 (S) TEM. Powder X-ray diffraction (XRD) patterns of unsupported samples (sonicated from NF) were collected at 40 kV and 40 mA with Cu Kα radiation (λ = 1.5406 Å). Characterization of the surface of the NF-supported samples was done by X-ray photoelectron spectroscopy (XPS) on a Thermo Scientific K-Alpha+ with Mono Al Kα radiation, The pressure in the analysis chamber was at around $5*10^{-9}$ mbar and the energy, voltage and beam current were 1486.6 eV, 12KV and 6 mA, respectively. The specific surface area and pore size distribution of the unsupported samples (collected precipitation with centrifugation after hydrothermal reaction) were obtained from N_2 adsorption/desorption isotherms on a Tristar II 3020 Micromeritics system. Fourier-transformed infrared (FT-IR) spectra of the unsupported samples(collected precipitation with centrifugation after hydrothermal reaction)were recorded on an Alpha Bruker spectrometer. The H_2 chemisorption tests of the unsupported samples (collected precipitation with centrifugation after hydrothermal reaction) were carried out on the Autochem HP system (Micromeritics Instrument Corp.).

2.4 Product quantification and calculation. To quantify the organic products, high-performance liquid chromatography (HPLC) was performed on an Agilent 1200 series at 30 °C. The HPLC was equipped with an ultraviolet-visible detector and Synergi 4u Polar-RP 80A 00G-4336-EO 250x4.60 mm column. The eluting solvents of A: 5% methanol, 0.4% phosphoric acid aqueous solution; and B: acetonitrile were utilized. The program was 15% solution B for 16 min, 25% solution B for 20 min and then 15% solution B for 16 min. The volume of injection was 5 μL. The flow rate was 0.5 mL s^{-1}. The calibration curves of standard chemicals were employed to determine and quantify the products. The quantification of the products by percentage conversion (Conv. %) of benzaldehyde (BZH) (1), average reaction rate (ARR) (2) and faraday efficiency (FE%) (3) without hydrogen evolution reaction consideration was carried out according to equations 1-3.

$$\text{Conv. [\%]} = \frac{moles\ of\ Benzaldehyde\ consumed}{initial\ moles\ of\ Benzaldehyde} \tag{1}$$

$$\text{ARR [µmol cm}^{-2}\text{ h}^{-1}] = \frac{moles\ of\ Benzaldehyde\ consumed}{area\ of\ working\ electrode * time} \tag{2}$$

$$\text{FE (\%)} = \frac{nZF}{Q} = \frac{electrons\ consumed\ by\ hydrogenation\ of\ organics}{Total\ electrons\ flowed\ through\ the\ system} \tag{3}$$

where n represents the number of moles of the target product, z the required electrons of this reaction z=2, and F the Faraday constant 96500 C· mol^{-1}.

2.5 Computational theoretical calculation. Inspired by the reported model of Ru@Ni-MOF[1], the analog structure of Pd@Ni-MOF was theoretically constructed, and the geometric optimization of the "Forcite" module was used to determine the structure and cell size of Pd and Ni-MOF. The adsorption energies for BZH with Pd@Ni-MOF were obtained by the "Sorption" and "Adsorption Locator" modules (the force field was COMPASS and the charge equilibrium was QEq). All density functional theory (DFT) calculations were performed using the Vienna ab initio simulation package (VASP), employing the projected augmented wave revising Perdew–Burke–Ernzerhof function (PAW−PBE). The cutoff energy was set at 500 eV for all the geometry optimizations. A 2 × 2 × 1 Monkhorst–Pack grid and A 4 × 3 × 2 Monkhorst–Pack grid were used to obtain the surface calculations on the Pd system and the Pd@Ni-MOF system, respectively. At least a 20 Å vacuum layer was applied in the z−direction of the slab models, preventing vertical interactions between slabs. The adsorption energy (E_{ads})

is described by equation 4 where $E_{(substrate/product\ and\ Pd)}$, $E_{(substrate/product)}$ and $E_{(Pd)}$ are the energies of the system involving the Pd (111) surface connecting the substrate/product, the only substrate/product, and the Pd surface, respectively. All structures were completely relaxed until the force on each atom was less than 0.01 eV Å^{-1}.

$$E_{ads} = E_{(substrate/product\ and\ Pd)} - E_{(substrate/product)} - E_{(Pd)} \tag{4}$$

The Free energy (E_{free}) was calculated using equation 5, ΔE, ΔZPE, and $T\Delta S$ are the changes in the internal energy E, zero point energy ZPE, and entropic energy TS, respectively. As an example, The Free energy (E_{free}) of elemental step *CHO→*CHO-H_3O shown in equation 6.[2]

$$\Delta G = \Delta E + \Delta ZPE - T\Delta S \tag{5}$$

$$E_{\mathrm{free}\ *\mathrm{CHO}\rightarrow *\mathrm{CHO}-H_3\mathrm{O}} = E_{free\ ^{*}\mathrm{CHOH}} - E_{free\ ^{*}\mathrm{CHO}-H_3\mathrm{O}} + E_{free\ ^{*}H_2\mathrm{O}} \tag{6}$$

2.6 Electrocatalytic hydrogenation tests: The electrochemical performance of the electrocatalyst was evaluated on a Corrtest CS2350 EIS Bipotentiostat (2-channel, Wuhan Corrtest Instrument Corp., Ltd) using an H-cell reactor divided by a Nafion 117 proton exchange membrane. The electrolyte was kept with pH=5.3 sodium acetate-acetic acid buffer solution. The prepared self-supported electrodes (cut into 3x1 cm^2 and keep 2x1 cm^2 immersed in the electrolyte) were used as the working electrode, a platinum mesh as the counter electrode, and an Ag/AgCl (KCl saturated) as the reference electrode. Cyclic voltammetry (CV) was performed in the range -1.1 V ~ 0.6 V vs. Ag/AgCl. Electrochemical impedance spectroscopy (EIS) was conducted at -0.4 V vs. Ag/AgCl. I-t curves were obtained by applying -0.6 V vs. Ag/AgCl as a constant voltage for 1 h or the following voltage sequence: -0.7 V vs. Ag/AgCl for 5 min, -0.65 V vs. Ag/AgCl for 5 min, -0.6 V vs. Ag/AgCl for 20 min, -0.55 V vs. Ag/AgCl for 20 min, and -0.5 V vs. Ag/AgCl for 10 min. Experiments were performed under constant N_2 flow.

3. Results and discussion

Pd nanoparticles supported on Ni-MOF-74 (Pd@Ni-MOF) were prepared by a one-step solvothermal process as shown in Scheme 1b (see details in the Experimental section). In this process, BDC, nickel(II) chloride hexahydrated, and palladium(II) acetate were used as the source of Ni-MOF and Pd, respectively. A NF was used as conducting support. A small amount of TEOA was employed as a morphology control agent to guarantee the good dispersion of Pd.

3.1 Structural, crystalline and chemical properties of Pd@Ni-MOF

Ni-MOF exhibits a three-dimensional architecture formed by intersecting nanosheets (Figs. 1a-c) that offers a large surface area for reactant adsorption and diffusion, ample pores for effective electrolyte diffusion, and a suitable solid network for fast charge transport. While in the absence of TEOA Pd strongly agglomerates (Fig. S1 and Table S1), the addition of a small amount of TEOA results in a homogeneous dispersion of Pd particles with an average diameter of 3 nm across the Ni-MOF surface as observed by TEM characterization (Figs. 1d, e). HRTEM micrographs of the Pd and the related fast Fourier transform (FFT) analysis displayed the Pd (111) plane with a 2.2 Å lattice spacing (Fig. 1f). The STEM-HAADF image and the associated EDS compositional maps of Pd@Ni-MOF confirmed the excellent dispersion of the different elements. Additionally, EDS analysis showed the Pd/Ni ratio within Pd@Ni-MOF to be 0.28 (Fig. 1g and Table S2).

The x-ray diffraction (XRD) patterns of Pd@Ni-MOF and Ni-MOF show peaks at 8.6°, 14.9°, 15.9º, and 17.1º, consistent with literature calculations of the Ni-MOF-74 crystal phase (Fig. S2).[23] On the other hand, the XRD peaks at 40.2º and 46.8º, only present in the Pd@Ni-MOF sample, are assigned to the metallic Pd phase.

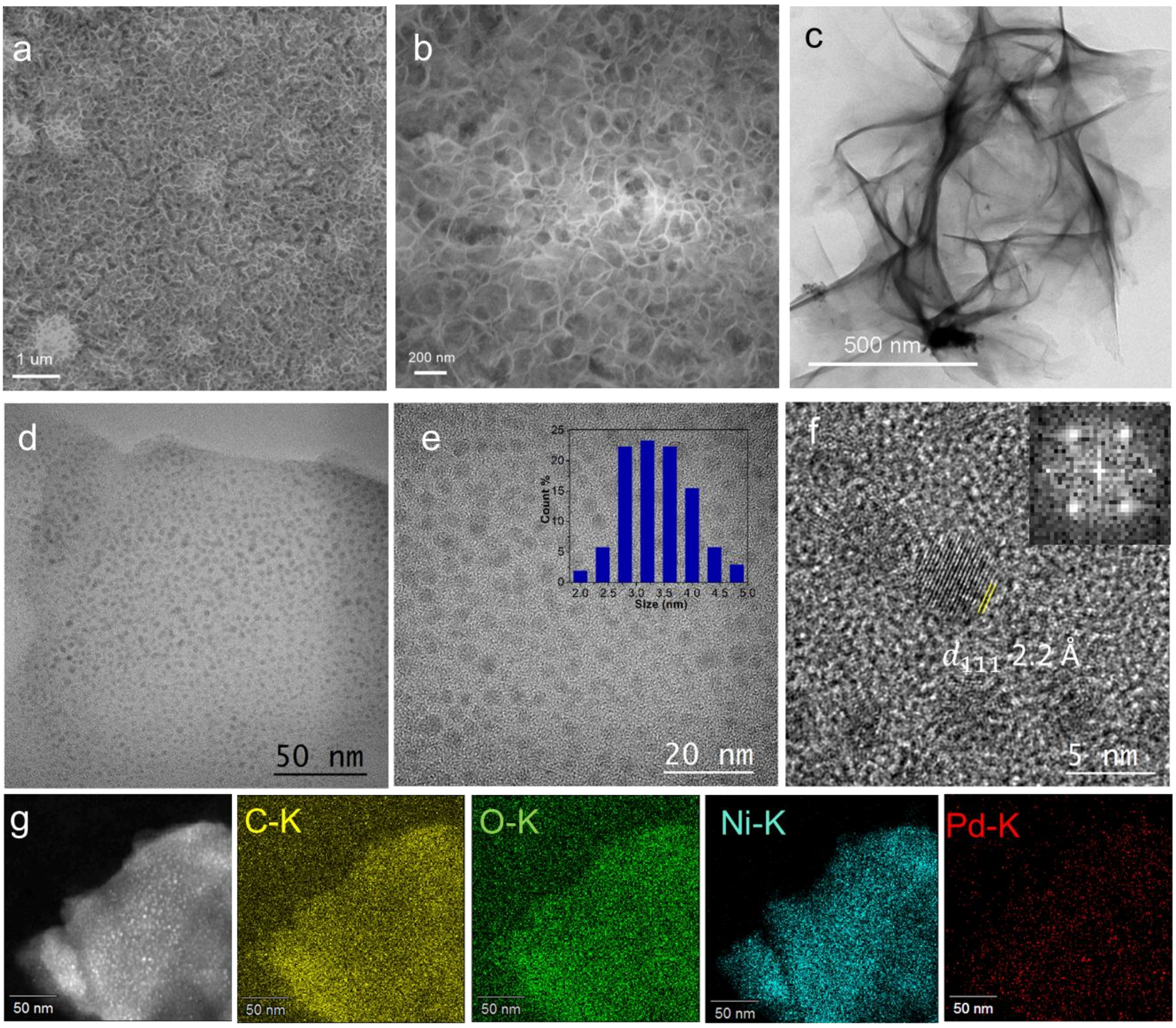

Fig. 1. Structural and chemical characterization of Pd@Ni-MOF. (a,b) SEM images. (c) Low-magnification TEM image. (d) High magnification TEM image; (e,f) HRTEM images and histogram with the size distribution of the Pd nanoparticles. (g) STEM-HAADF image and compositional maps: yellow = C; green = O; blue = Ni; red = Pd.

The specific surface area of Pd@Ni-MOF and Ni-MOF were quantified at 30.3 $m^2 \cdot g^{-1}$, and 31.6 $m^2 \cdot g^{-1}$, respectively (Fig. S3). Thus, the presence of Pd did not significantly modify the surface area of the Ni-MOF. The organic framework of the material was characterized using FTIR. The

IR absorption peaks at 1575 and 1357 cm^{-1} are associated with the benzene ring skeleton stretching vibration splitting peaks, indicating the presence of an aromatic ring structure in the organic framework (Fig. S4). The absorption peaks at 1636 cm^{-1} and 1422 cm^{-1} provide from the antisymmetric and symmetric stretching vibration peaks of carboxylate (COO), respectively. The difference $\Delta [\nu_{as} - \nu_{s}]$ is about 214 cm^{-1}, indicating that the carboxyl group of 1,4-BDC and the Ni ion form a bond through bridge coordination.[24-26]

Fig. 2 shows the high-resolution Pd 3d, Ni 2p, O 1s, and C 1s XPS spectra of Pd@Ni-MOF, Ni-MOF and a reference 20% Pd@C sample. The Pd 3d spectrum of Pd@Ni-MOF shows a doublet at 342.4 eV (Pd $3d_{3/2}$) and 337.1 eV (Pd $3d_{5/2}$) assigned to a Pd-O chemical environment. In the reference 20% Pd@C sample, peaks located at 341.1 eV (Pd $3d_{3/2}$) and 335.8 eV (Pd $3d_{5/2}$) are assigned to Pd^0. Besides the satellite peaks, the Ni 2p XPS spectrum of Pd@Ni-MOF also shows one doublet at 873.0 eV (Ni $2p_{1/2}$) and 855.6 eV (Ni $2p_{3/2}$) assigned to a Ni^{2+} chemical environment. A very similar spectrum was obtained from the Ni-MOF sample. The O 1s spectrum shows several contributions tentatively assigned to Ni-O-Pd (529.1eV), Ni-O-Ni (530.8 eV) of MOF, O=C-O (531.6 eV) of the linker in MOF and H_2O (532.6 eV).

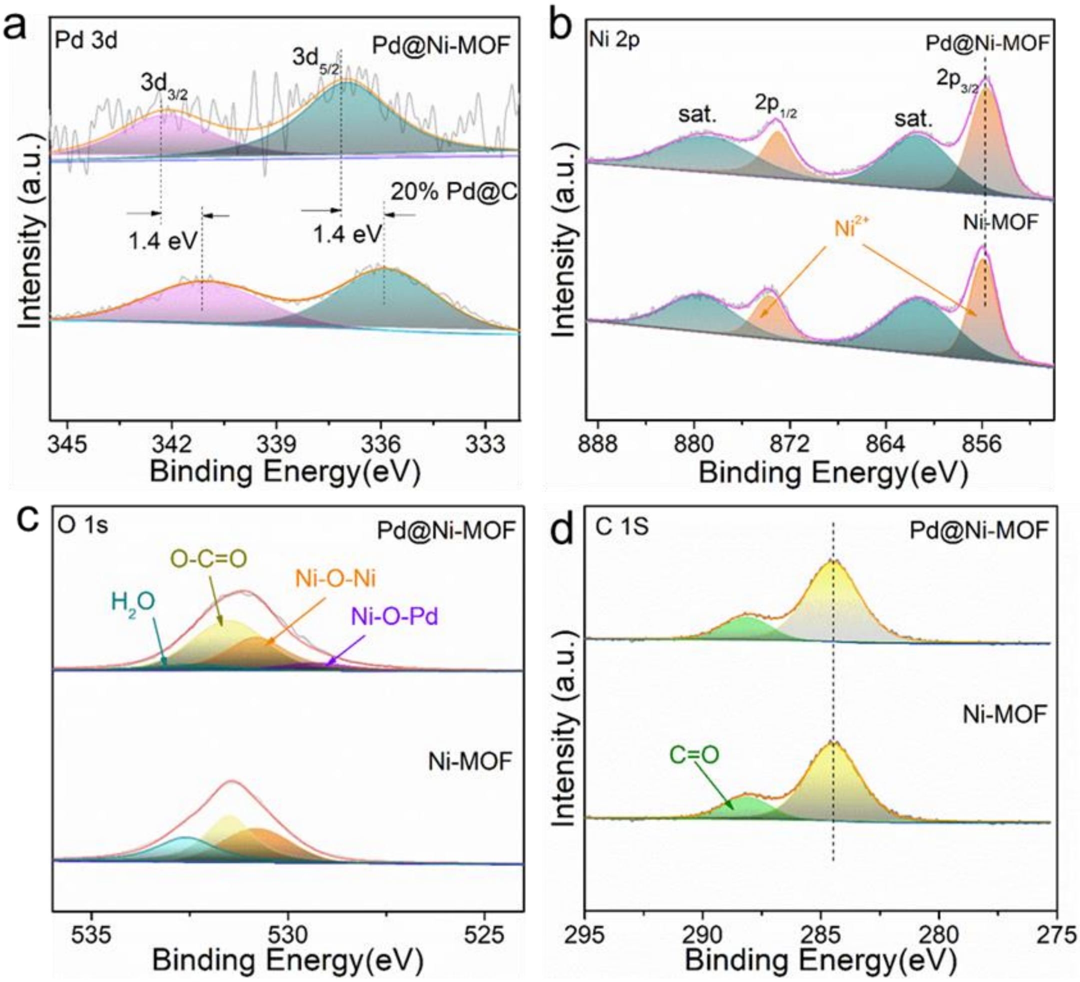

Fig. 2. High-resolution XPS spectra of Pd@Ni-MOF, 20 % Pd@C and Ni-MOF, as indicated in each panel: (a) Pd 3d; b) Ni 2p; c) O 1s; and (d) C 1s.

3.2 Electrochemical performances of Pd@Ni-MOF

CV curves in 3 M pH 5.2 sodium acetate-acetic acid buffer solution electrolyte are shown in Fig. 3a (blue line). In the reverse scan, the CV curve shows a shoulder at -0.24 V vs. Ag/AgCl, overlapping with the hydrogen evolution reaction (HER) taking place at potentials below -0.3 V vs. Ag/AgCl. This shoulder, usually referred to as the hydrogen underpotential deposition (H_{upd}) region, is assigned to the hydrogen adsorption and the formation of Pd hydride (Pd-H). In the forward scan, the large peak at -0.03 V vs. Ag/AgCl is assigned to the hydrogen desorption.

When adding BZH into the electrolyte, in the forward scan, the hydrogen desorption peak massively shrank. In parallel, in the reverse scan, the shoulder disappeared and the step increase related to HER decreases. This is associated with the onset potential of BZH hydrogenation being comparable with HER but the kinetics of the BZH hydrogenation reaction being slower than that of HER. This slower BZH hydrogenation kinetics is also reflected in the much larger Tafel slope in the presence of BZH, 137 mV dec^{-1}, than in its absence (41 mV dec^{-1}, Fig. 3b).

The reversible adsorption of hydrogen, $H_{upd} \rightleftharpoons H^+(aq) + e^- + *$, dominating the CV curve in an acid electrolyte is commonly used to estimate the number of adsorption sites. Because the H_{upd} overlaps with HER, the hydrogen desorption peak in the forward scan is generally used for this estimation. As shown in the CV curves in Fig. S5, the presence of larger amounts of BZH progressively inhibits hydrogen deposition, which translates into the area of the hydrogen desorption peak S_H decreasing with the introduction of increasing amounts of the organic molecule. Fig. S5b shows the H_{upd} deposition/desorption region of the CV for Pd@Ni-MOF in acetate buffer (pH 5.2) and with different concentrations of BZH. Under the assumption that only BZH and hydrogen adsorb on the surface active sites of the electrocatalyst,[27-29] that both species occupy all the active sites, with hydrogen atoms occupying the complete active sites in the pure electrolyte,[27] while disregarding the effect of the double-layer capacitance[30] and also assuming the desorption of BZH does not affect the H desorption peak area,[31] it is possible to determine the hydrogen coverage (θ_H) and BZH coverage (θ_{BZH}) through:

$$\theta_H = \frac{Area\ of\ the\ H\ desorption\ region}{Area\ of\ H\ desorption\ region\ in\ pure\ electrolyte} \tag{1}$$

$$\theta_{BZH} = 1 - \theta_H \tag{2}$$

Adding 20 mM of BZH into the electrolyte, S_H strongly decreased, from 18.7 mA·V to 7.0 mA·V and $\theta_{Hydrogen}$ declined from 1 in the pure electrolyte to 0.38. In contrast, the S_H of commercial 20% Pd@C was not substantially affected with the introduction of BZH, from 0.20 mA·V to 0.22 mA·V, with $\theta_{Hydrogen}$ maintained at almost 1. On the other hand, the TEOA-free Pd@Ni-MOF also underwent a notable S_H change, from 17.9 mA·V to 7.6 mA·V, reaching a $\theta_{Hydrogen}$ of 0.42. In addition, the Ni-MOF showed a notable S_H change from 5.0 mA·V to 3.5 mA·V, and a $\theta_{Hydrogen}$ reduction to 0.72, which indicates that the Ni-MOF plays a role in the adsorption of BZH. These experimental results demonstrate that Pd@Ni-MOF electrodes are much more prone to adsorb BZH than the commercial 20% Pd@C catalyst. Besides, as reflected by the dependence of S_H on the BZH concentration (Fig. 3c), at all BZH concentrations, hydrogen adsorption still takes place, thus both species are simultaneously adsorbed, which is key for the BZH hydrogenation to take place.

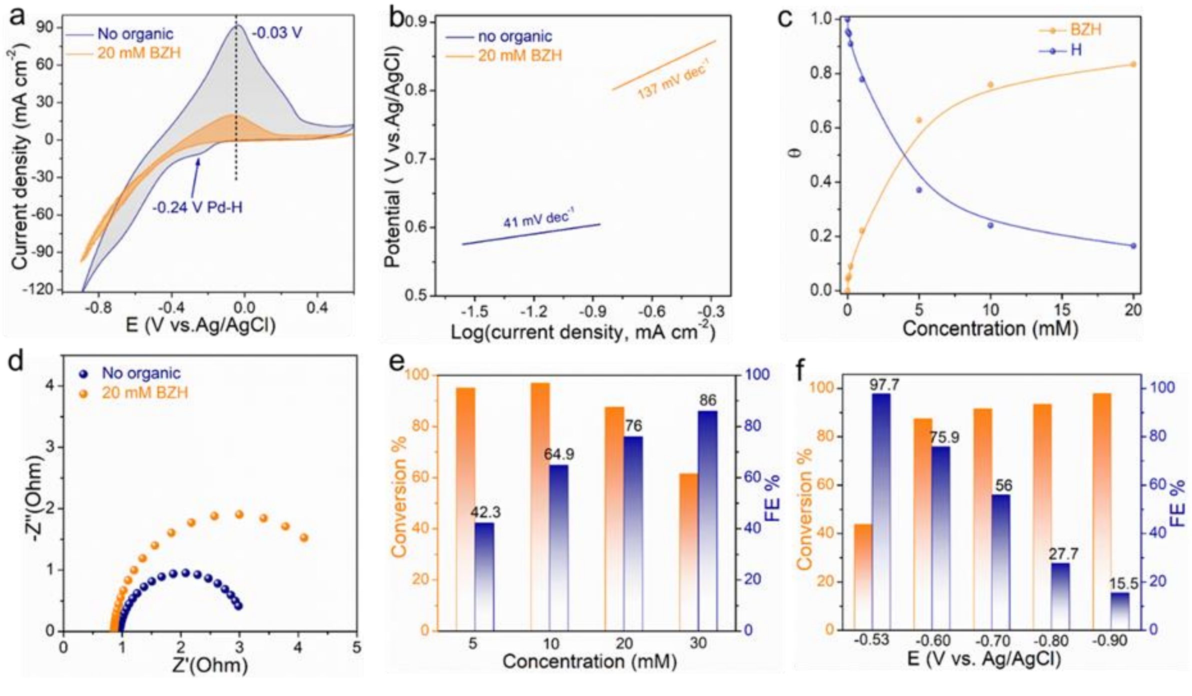

Fig. 3. (a) Cyclic voltammetry curves of Pd@Ni-MOF in the presence and absence of 20 mM BZH. (b) Tafel plot. (c) H and BZH surface coverage. (d) Nyquist plot of the EIS spectra in the presence and absence of 20 mM BZH. (e) BZH-to-BA conversion and FE as a function of the BZH concentration at

constant voltage -0.6 V vs. Ag/AgCl; (f) BZH-to-BA conversion and FE as a function of the voltages with 20 mM BZH.

Fig. 3c displays the Nyiquist plot of the EIS spectra of the Pd@Ni-MOF electrode in the blank electrolyte and the presence of BZH. Comparing the different materials (Fig. S6), we observe the charge transfer resistance without BZH to be the lowest for Pd@Ni-MOF (~2 Ω), well below that of Pd@C (~48 Ω) and TEOA-free Pd@Ni-MOF (~4 Ω). As expected, a larger semicircle is obtained in the presence of BZH, associated with the inhibition of the HER and the related higher charge transfer resistance at the electrolyte/electrode interphase. In contrast, the Ni-MOF shows a much larger resistance (>1000 Ω) which is not significantly affected by the presence of BZH, demonstrating its role just as support of the active component.

The Faradaic efficiencies (FEs) of the ECH of BZH over Pd@Ni-MOF were determined after 1h of reaction at a constant voltage of -0.6 V vs. Ag/AgCl using different substrate concentrations (Fig. 3e). The FE increased as the BZH concentration increased, up to 86% for a 30 mM BZH. This correlation of the FE with the BZH concentration is related to the increase in the BZH coverage and the consequent reduction of H coverage that reduces the competing HER activity. Fig. 3f shows the conversion and FE after 1h reaction at different voltages at a set concentration. The FE rapidly decreases as the voltage increases, which is related to the H_2 bubbles generated by the stronger HER, inhibiting BZH adsorption and thus its hydrogenation. Notice that while high FE up to 98% were obtained at low voltages (-0.53 V vs. Ag/AgCl), the conversion after 1h reaction in these conditions was moderate (just 42% at -0.53 V vs. Ag/AgCl).

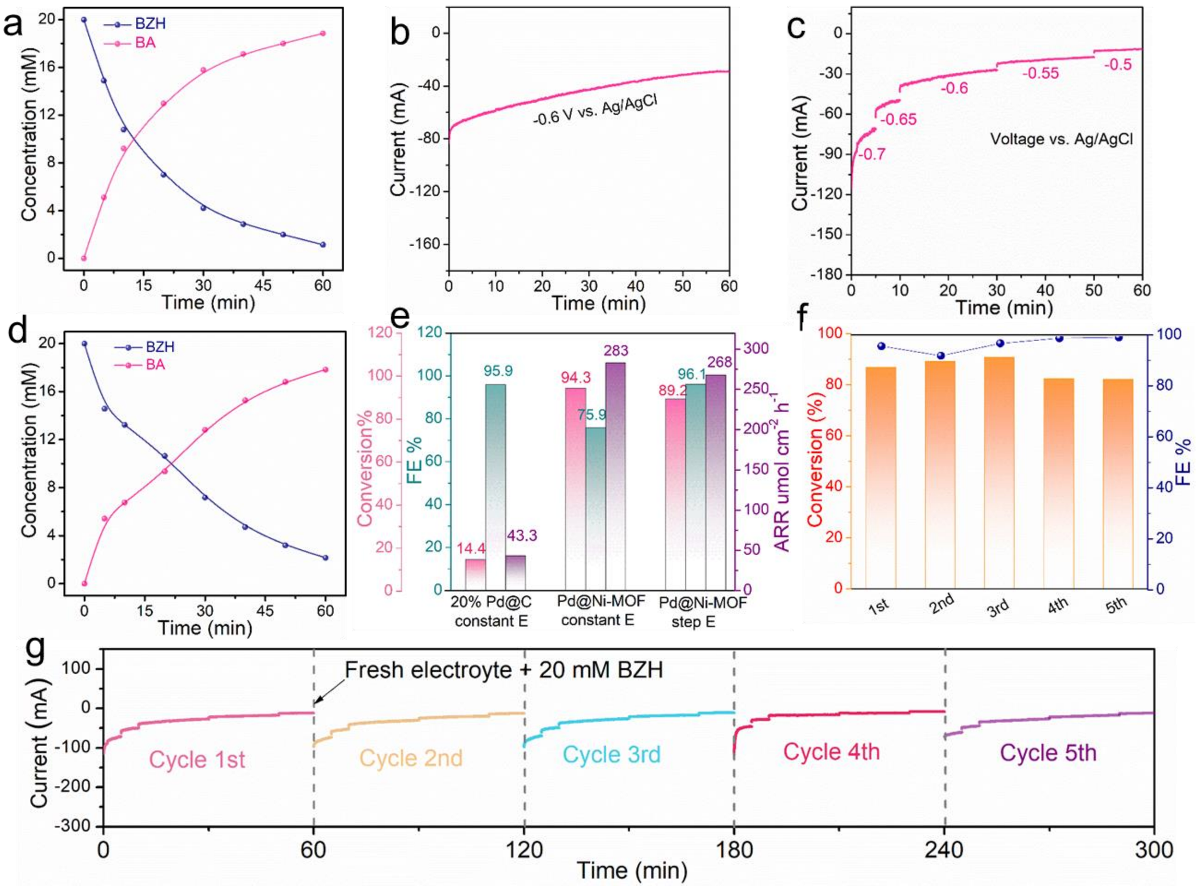

Fig. 4. Time-dependent conversion of BZH to BA over Pd@Ni-MOF. (a) BZH conversion and BA production at a constant voltage of -0.6 vs Ag/AgCl. (b) I-t curve at -0.6 vs Ag/AgCl. (c) I-t profile under a progressively decreasing voltage. (d) BZH conversion and BA production using the voltage steps displayed in panel c. (e) Comparison of the conversion, FE and ARR of different catalysts and strategies; (f) BZH to BA conversion and FE for 5 cycles with a stepped voltage. (g) I-t profile of the BZH to BA conversion for 5 cycles with a step voltage.

The time-dependence transformation of BZH into BA over Pd@Ni-MOF when applying a constant voltage -0.6V vs. Ag/AgCl is shown in Fig. 4a, we observe that in the batch H-cell reactors, as the reaction proceeds, the concentration of BZH rapidly decreases. The related I-t curve (Fig. 4b) exhibited a current density decrease as the reaction proceeded. This result is related to an indirect reduction mechanism where the adsorbed BZH reacts with the reduced H_{ad} atoms rather than accepting electrons and reacting with H^+. Notably, Fig. S8 exhibits the I-t curves at different voltages of conversion of BZH to BA over Pd@Ni-MOF showing that the I-t curve at -0.9 V vs. Ag/AgCl presents a remarkable current increase as corresponds to a direct reduction process in competition with HER. [32]

To maximize the FE, we considered a progressive reduction of the applied voltage as the concentration of the substrate decreases, as shown in the I-t profile of Fig. 4c. Fig. 4d shows the time dependence of the conversion obtained using this step voltage function. This strategy allowed reaching FE above 96 % with a total conversion of 88% after 1h reaction (Fig. 4e). Such high FEs could be maintained over five 60 min cycles, as shown in Fig. 4f and Fig. 4g.

The XRD patterns (Fig. S9) of the powders obtained from the sonication of the electrode after five cycles for a total of 300 min of reaction show the Ni-MOF fingerprint has disappeared. This result shows a partial amorphization of the MOF during the reaction, but without a major morphology and elemental distribution change according to SEM and HAADF-EDS analysis (Fig. S10). Compared with the fresh Pd@Ni-MOF electrocatalyst (Table S1), EDX analysis (Table S4) of the catalyst powder after cycling shows the amount of Ni to have decreased from 10.3% to 5.4% while the relative amount of Pd has significantly increased from 2.9% up to 7.4 %. XPS spectra of the Pd@Ni-MOF after cycling (Fig. S11) display no major change in the Pd 3d XPS spectrum after cycling, with the main peaks being associated with Pd^0 (3d $_{5/2}$ 335.1 eV and 3d $_{3/2}$ 341.9 eV), which indicate that in the operating reduction condition, some of the Pd^{2+} was reduced to Pd^0. The Ni/Pd ratio obtained by XPS significantly decreased with the reaction, consistently with EDX data. We associate this decrease with the partial leaching of Ni ions in the acid electrolyte. Notice that according to the stability test data shown in Fig. 4g, this leaching had a minor effect on the performance.

3.3 Adsorption configuration of BZH on Pd@Ni-MOF

To understand the high activity of Pd@Ni-MOF, the adsorption process was simulated using

Materials Studio (MS) calculations. ECH reactions are generally supported by a proton-coupled electron transfer (PCET) mechanism. In this two-electron process, a proton is reduced or an H_2 molecule is dissociated to form an adsorbed hydrogen (H_{ads}) that reacts with the adsorbed organic molecule. It is thus essential that the catalyst surface offers sites for the simultaneous adsorption of both the organic molecule, BZH in this case, and H. On a pure Pd surface, the BZH tends to be adsorbed through the phenyl ring with a vertical configuration.[33] When Pd nanoparticles are dispersed on a graphitic carbon support, the phenyl ring structure drives the adsorption of BZH with a horizontal or vertical configuration (Figs. S12a,b). On the other hand, Pd nanoparticles bind to the oxygen-rich Ni-MOF through surface oxygen (Pd-O-Ni), accepting electrons provided by the oxygen in the MOF structure. In this scenario, Pd becomes an electron acceptor and the reduced electron cloud density around Pd enables BZH to adsorb on its surface through the carbonyl group rather than the phenyl ring, thus the titled adsorption configuration becomes the most favorable (Fig. S12c). In this configuration, the total average energy of BZH adsorbed on Pd@Ni-MOF is -64.11 kcal/mol, well above (in absolute value) that of BZH adsorbed on Pd@C, at -50.47 kcal/mol.

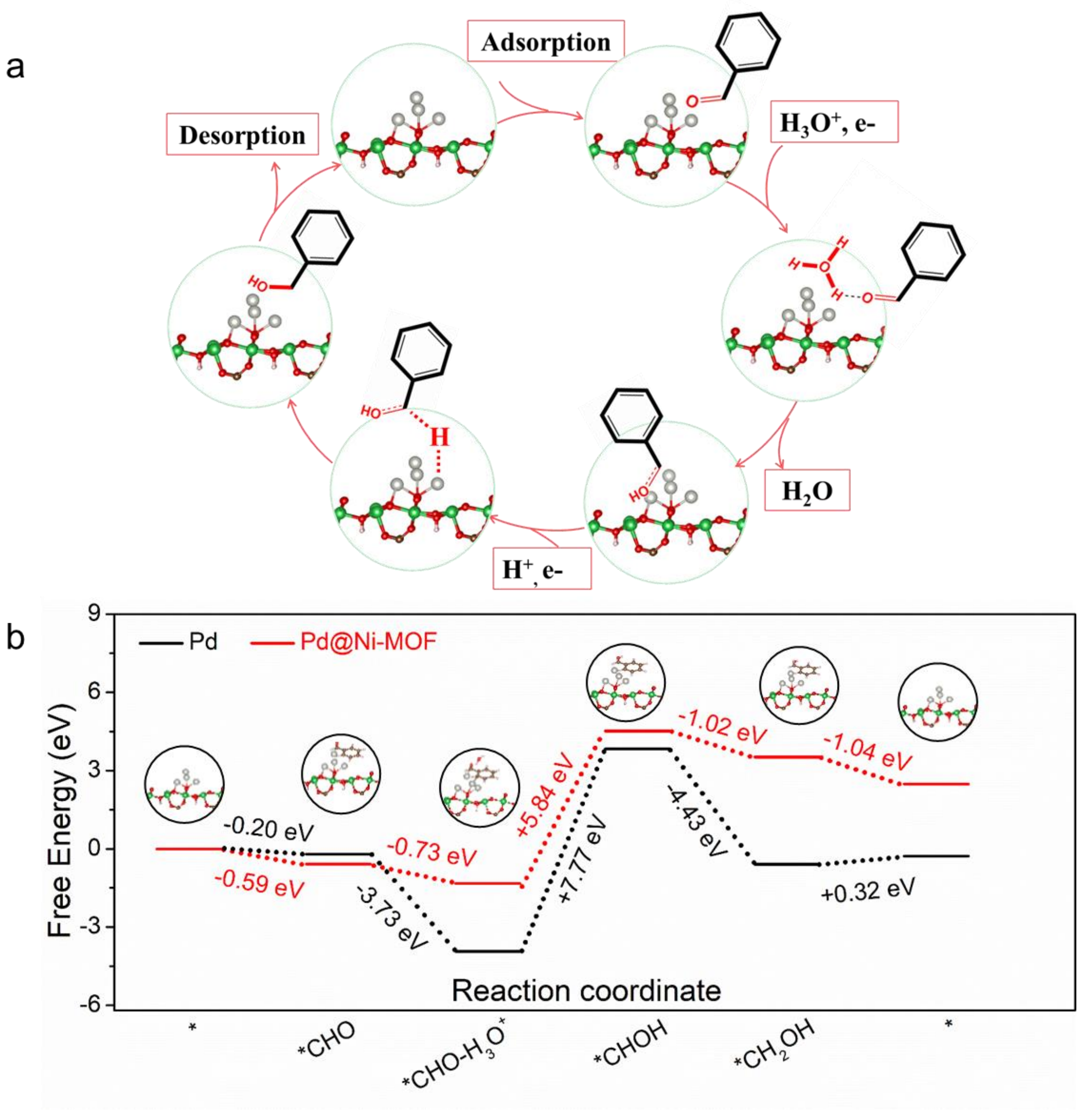

Fig. 5. (a) Proton-coupled electron transfer mechanism of the ECH of BZH to BA. Grey ball for Pd, Green for Ni, red for O, wine for C. (b) Free energy profiles for the BZH-to-BA process on Pd and Pd@Ni-MOF.

Based on the initial simulation results showing the tilted adsorption configuration of BZH on the material Pd@Ni-MOF, DFT calculations were carried out to determine adsorption energies of the substrate, intermediates and product on the surface of Pd (Fig. S13) and Pd@Ni-MOF(Fig. S14). We considered the overall ECH reaction:

$$phCHO + 2H^{+} + 2e^{-} \rightarrow phCH_{2}OH \tag{3}$$

involving the following elementary steps (Fig. 5a):

$$phCHO + * \overset{1}{\rightarrow} phCHO * \tag{4}$$

$$phCHO * + H_3O^+ + e^- \overset{2}{\rightarrow} phCHOH_3O * \tag{5}$$

$$phCHOH_3O * \overset{3}{\rightarrow} phCHOH * + H_2O \tag{6}$$

$$H^+ + e^- + * \overset{4}{\rightarrow} H_{Ads} \tag{7}$$

$$phCHOH * + H_{Ads} \overset{5}{\rightarrow} phCH_2OH * \tag{8}$$

$$phCH_2OH * \overset{6}{\rightarrow} phCH_2OH + * \tag{9}$$

Fig. 5b displays the free energy change from the substrate phCHO, intermediate species phCHO-H_3O, phCHOH, and the product $phCH_2OH$ on unsupported Pd and Pd@Ni-MOF. The substrate adsorption step indicates a stronger BZH energy on the surface of Pd@Ni-MOF (-0.59 eV) than on Pd (-0.20 eV). The most prominent advantage of the Pd@Ni-MOF is the lower free energy change associated with the H_2O molecule removal step, which is the rate-limiting step. The free energy change associated with this step in Pd@Ni-MOF is +5.84 eV, well above the value obtained for unsupported Pd, +7.77 eV. This lower energy change is related to the formation of Pd-O-Ni bonds on the Ni-MOF surface that changes Pd from an electron donor to an electron acceptor, thus facilitating the removal of H_2O molecules. The free energy of the second hydrogen atom added to the species phCHOH (6) is higher on Pd@Ni-MOF (-1.02 eV) than on the Pd surface (-4.43 eV), which decreases the kinetic energy barrier significantly.

4. Conclusion

A Pd@Ni-MOF electrocatalyst containing a uniform dispersion of Pd particles on the surface of a Ni-MOF was produced and characterized. This electrocatalyst showed excellent activity toward the BZH ECH to BA in an aqueous phase, with an outstanding ECH rate of up to 283 μmol cm^{-2} h^{-1} with a FE of 76%. This excellent performance is related to the important role played by the Ni-MOF in increasing the adsorbed hydrogen coverage, enabling the tilted adsorption of BZH through its carbonyl group, and facilitating H_2O desorption. Besides, we demonstrate the reaction FE can be increased up to 96 % by modulating the applied voltage while the total conversion is improved to close to 90%. In this strategy, relatively high voltages are applied at high substrate concentrations and are decreased as the concentration decreases to maintain a high selectivity. This work provides new insight into the selective hydrogenation of BZH into monomer-alcohol products and other carbonyl functional group organics.

Acknowledgements

L. Gong (CSC No.: 202106180029) and C.Y. Zhang (CSC No.: 202106180045) thank the China Scholarship Council for the scholarship support. This work was supported by the Innovation fund for small and Medium-sized Enterprises in Gansu Province (No.22CX3JA006), Lanzhou Talent Innovation and Entrepreneurship Project (No.2022-2-81) partially by the Fundamental Research Funds for the Central Universities (Grant Nos.: lzujbky−2021−it33). The authors greatly acknowledge the support of the Supercomputing Center of Lanzhou University, China. J. Li is grateful for the project supported by the Natural Science Foundation of Sichuan Province (2022NSFSC1229). The authors also greatly thank for the generous help from Liming Deng and Professor Dr. Shengjie Peng (College of Materials Science and Technology Nanjing University of Aeronautics and Astronautics Nanjing 210016, China). The project on which these results are based has received funding from the European Union's Horizon 2020 research and innovation programme under Marie Skłodowska-Curie grant agreement No. 801342 (Tecniospring INDUSTRY) and the Government of Catalonia's Agency for Business Competitiveness (ACCIÓ). The authors acknowledge funding from Generalitat de Catalunya 2021SGR00457. ICN2 acknowledges funding from project PID2020-116093RB-C43, funded by MCIN/AEI/10.13039/501100011033/ and by “ERDF A way of making Europe”, by the “European Union”. This study was supported by MCIN with funding from European Union NextGenerationEU (PRTR-C17.I1) and Generalitat de Catalunya. ICN2 is supported by the Severo Ochoa program from Spanish MCIN / AEI (Grant No.: CEX2021-001214-S). ICN2 and IREC are funded by the CERCA Programme/Generalitat de Catalunya. Part of the present work has been performed in the framework of Universitat Autònoma de Barcelona Materials Science PhD program. M.B. acknowledges support from SUR Generalitat de Catalunya and the EU Social Fund; project ref. 2020 FI 00103.

Declaration of Competing Interest

The authors declare no conflict of interest.

Reference and notes

[1] M. Talebi Amiri, G.R. Dick, Y.M. Questell-Santiago, J.S. Luterbacher, Fractionation of lignocellulosic biomass to produce uncondensed aldehyde-stabilized lignin, Nat. Protoc., 14 (2019) 921-954.

[2] M.P. Pandey, C.S. Kim, Lignin Depolymerization and Conversion: A Review of Thermochemical Methods, Chem. Eng. Technol., 34 (2011) 29-41.

[3] D.C. Cantu, A.B. Padmaperuma, M.-T. Nguyen, S.A. Akhade, Y. Yoon, Y.-G. Wang, M.-S.

Lee, V.-A. Glezakou, R. Rousseau, M.A. Lilga, A Combined Experimental and Theoretical Study on the Activity and Selectivity of the Electrocatalytic Hydrogenation of Aldehydes, ACS Catal., 8 (2018) 7645-7658.

[4] U. Sanyal, K. Koh, L.C. Meyer, A. Karkamkar, O.Y. Gutiérrez, Simultaneous electrocatalytic hydrogenation of aldehydes and phenol over carbon-supported metals, J. Appl. Electrochem., 51 (2021) 27-36.

[5] S.A. Akhade, N. Singh, O.Y. Gutiérrez, J. Lopez-Ruiz, H. Wang, J.D. Holladay, Y. Liu, A. Karkamkar, R.S. Weber, A.B. Padmaperuma, M.-S. Lee, G.A. Whyatt, M. Elliott, J.E. Holladay, J.L. Male, J.A. Lercher, R. Rousseau, V.-A. Glezakou, Electrocatalytic Hydrogenation of Biomass-Derived Organics: A Review, Chem. Rev., 120 (2020) 11370-11419.

[6] Y.P. Wijaya, K.J. Smith, C.S. Kim, E.L. Gyenge, Electrocatalytic hydrogenation and depolymerization pathways for lignin valorization: toward mild synthesis of chemicals and fuels from biomass, Green Chem., 22 (2020) 7233-7264.

[7] K. Li, Y. Sun, Electrocatalytic Upgrading of Biomass-Derived Intermediate Compounds to Value-Added Products, Chem. Eur. J., 24 (2018) 18258-18270.

[8] J. Li, L. Li, X. Ma, X. Han, C. Xing, X. Qi, R. He, J. Arbiol, H. Pan, J. Zhao, J. Deng, Y. Zhang, Y. Yang, A. Cabot, Selective Ethylene Glycol Oxidation to Formate on Nickel Selenide with Simultaneous Evolution of Hydrogen, Adv. Sci., n/a (2023) 2300841.

[9] J. Li, X. Tian, X. Wang, T. Zhang, M.C. Spadaro, J. Arbiol, L. Li, Y. Zuo, A. Cabot, Electrochemical Conversion of Alcohols into Acidic Commodities on Nickel Sulfide Nanoparticles, Inorg. Chem., 61 (2022) 13433-13441.

[10] J.T. Bhanushali, I. Kainthla, R.S. Keri, B.M. Nagaraja, Catalytic Hydrogenation of

Benzaldehyde for Selective Synthesis of Benzyl Alcohol: A Review, ChemistrySelect, 1 (2016) 3839-3853.

[11] C.J.C. Rodrigues, C.C.C.R. de Carvalho, Process Development for Benzyl Alcohol Production by Whole-Cell Biocatalysis in Stirred and Packed Bed Reactors, Microorganisms, 2022.

[12] Y. Yang, W.-Y. Song, H.-G. Hur, T.-Y. Kim, S. Ghatge, Thermoalkaliphilic laccase treatment for enhanced production of high-value benzaldehyde chemicals from lignin, Int. J. Biol. Macromol., 124 (2019) 200-208.

[13] Y. Song, U. Sanyal, D. Pangotra, J.D. Holladay, D.M. Camaioni, O.Y. Gutiérrez, J.A. Lercher, Hydrogenation of benzaldehyde via electrocatalysis and thermal catalysis on carbon-supported metals, J. Catal., 359 (2018) 68-75.

[14] J.A. Lopez-Ruiz, E. Andrews, S.A. Akhade, M.-S. Lee, K. Koh, U. Sanyal, S.F. Yuk, A.J. Karkamkar, M.A. Derewinski, J. Holladay, V.-A. Glezakou, R. Rousseau, O.Y. Gutiérrez, J.D. Holladay, Understanding the Role of Metal and Molecular Structure on the Electrocatalytic Hydrogenation of Oxygenated Organic Compounds, ACS Catal., 9 (2019) 9964-9972.

[15] Q. Yang, F. Yao, Y. Zhong, F. Chen, X. Shu, J. Sun, L. He, B. Wu, K. Hou, D. Wang, X. Li, Metal – Organic Framework Supported Palladium Nanoparticles: Applications and Mechanisms, Part. Part. Syst. Charact., 36 (2019) 1800557.

[16] S. Mukhopadhyay, O. Basu, R. Nasani, S.K. Das, Evolution of metal organic frameworks as electrocatalysts for water oxidation, Chem. Commun., 56 (2020) 11735-11748.

[17] A. Dhakshinamoorthy, A.M. Asiri, H. Garcia, 2D Metal–Organic Frameworks as Multifunctional Materials in Heterogeneous Catalysis and Electro/Photocatalysis, Adv. Mater.,

31 (2019) 1900617.

[18] Y. Deng, P. Yuan, X. Yuan, J. Wu, H.-A. Luo, Preparation of Hydrophobic Cosalen/SBA-15 and Its Application in the Selective Oxidation of Toluene, Chem J Chin Univ-Chin, 34 (2013) 2617-2622.

[19] Y. Wu, Z. Guo, C. Sun, X. Ren, Q. Li, High-efficiency electrochemical hydrogenation of biomass-derived benzaldehyde compounds via a durable and versatile dendritic-like Pd/Cu-CF electrocatalyst, Fuel Process. Technol., 237 (2022) 107436.

[20] A.K. Vasiliou, J.H. Kim, T.K. Ormond, K.M. Piech, K.N. Urness, A.M. Scheer, D.J. Robichaud, C. Mukarakate, M.R. Nimlos, J.W. Daily, Q. Guan, H.-H. Carstensen, G.B. Ellison, Biomass pyrolysis: Thermal decomposition mechanisms of furfural and benzaldehyde, J. Chem. Phys., 139 (2013) 104310.

[21] J. Wu, D. Liang, X. Song, T. Liu, T. Xu, S. Wang, Y. Zou, Sulfonic groups functionalized Zr-metal organic framework for highly catalytic transfer hydrogenation of furfural to furfuryl alcohol, J. Energy Chem., 71 (2022) 411-417.

[22] K. Koh, U. Sanyal, M.-S. Lee, G. Cheng, M. Song, V.-A. Glezakou, Y. Liu, D. Li, R. Rousseau, O.Y. Gutiérrez, A. Karkamkar, M. Derewinski, J.A. Lercher, Electrochemically Tunable Proton-Coupled Electron Transfer in Pd-Catalyzed Benzaldehyde Hydrogenation, Angew. Chem. Int. Ed. Engl., 59 (2020) 1501-1505.

[23] L. Deng, F. Hu, M. Ma, S.-C. Huang, Y. Xiong, H.-Y. Chen, L. Li, S. Peng, Electronic Modulation Caused by Interfacial Ni-O-M (M=Ru, Ir, Pd) Bonding for Accelerating Hydrogen Evolution Kinetics, Angew. Chem. Int. Ed. Engl., 60 (2021) 22276-22282.

[24] Z. Gao, Y. Lai, L. Zhang, Y. Lin, L. Xiao, Y. Luo, F. Luo, Synthesis, Characterization, and

Electrocatalytic Activity Exploration of MOF-74: A Research-Style Laboratory Experiment, J. Chem. Educ., 98 (2021) 3341-3347.

[25] A. Vimont, J.-M. Goupil, J.-C. Lavalley, M. Daturi, S. Surblé, C. Serre, F. Millange, G. Férey, N. Audebrand, Investigation of Acid Sites in a Zeotypic Giant Pores Chromium(III) Carboxylate, J. Am. Chem. Soc., 128 (2006) 3218-3227.

[26] H. Jiang, Q. Wang, H. Wang, Y. Chen, M. Zhang, MOF-74 as an Efficient Catalyst for the Low-Temperature Selective Catalytic Reduction of NO_x with NH_3, ACS Appl. Mater. Interfaces, 8 (2016) 26817-26826.

[27] N. Singh, U. Sanyal, J.L. Fulton, O.Y. Gutiérrez, J.A. Lercher, C.T. Campbell, Quantifying Adsorption of Organic Molecules on Platinum in Aqueous Phase by Hydrogen Site Blocking and in Situ X-ray Absorption Spectroscopy, ACS Catal., 9 (2019) 6869-6881.

[28] J. Akinola, I. Barth, B.R. Goldsmith, N. Singh, Adsorption Energies of Oxygenated Aromatics and Organics on Rhodium and Platinum in Aqueous Phase, ACS Catal., 10 (2020) 4929-4941.

[29] M.A. Villalba, M.T.M. Koper, Structure Sensitivity of Acetophenone Reduction on Palladium-Modified Platinum Single-Crystal Electrodes, J. Phys. Chem. C, 124 (2020) 25884-25891.

[30] D.A. Stevens, J.R. Dahn, Electrochemical Characterization of the Active Surface in Carbon-Supported Platinum Electrocatalysts for PEM Fuel Cells, J. Electrochem. Soc., 150 (2003) A770.

[31] X. Wang, Y. Jiao, L. Li, Y. Zheng, S.-Z. Qiao, Local Environment Determined Reactant Adsorption Configuration for Enhanced Electrocatalytic Acetone Hydrogenation to Propane,

Angew. Chem. Int. Ed. Engl., 61 (2022) e202114253.

[32] A.M. Polcaro, S. Palmas, S. Dernini, Electrochemical reduction of carbonyl compounds at modified carbon felt electrodes, Electrochim. Acta, 38 (1993) 199-203.

[33] C.J. Bondue, M.T.M. Koper, Electrochemical Reduction of the Carbonyl Functional Group: The Importance of Adsorption Geometry, Molecular Structure, and Electrode Surface Structure, J. Am. Chem. Soc., 141 (2019) 12071-12078.

Graphical abstract

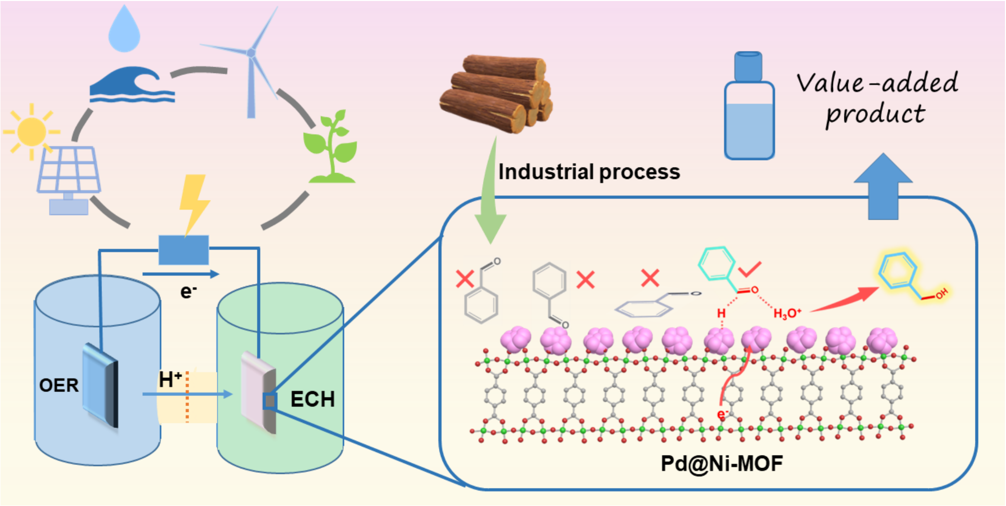

Highlights

1. Production and characterization of Pd particles on the surface of a Ni-MOF material.
2. Excellent activity toward the electrohydrogenation of benzaldehyde to benzyl alcohol in an aqueous phase.
3. Ni-MOF increased the adsorbed hydrogen coverage, enabling the tilted adsorption of benzaldehyde and facilitated elementary step.

Supporting Information

Enhanced Electrochemical Hydrogenation of Benzaldehyde to Benzyl Alcohol on Pd@Ni-MOF by Modifying the Adsorption Configuration

Li Gong[a,b], Chaoyue Zhang[a,c]*, Junshan Li [d], Guillem Montaña-Mora[a,b], Marc Botifoll[e], Jordi Arbiol[e], Jinyuan Zhou[c], Tanja Kallio[g], Paulina R. Martínez-Alanis[a,b]*, Andreu Cabot[a,f]*

[a]Catalonia Institute for Energy Research – IREC Sant Adrià de Besòs, Barcelona 08930, Spain E-mail: pmartinez@irec.cat, acabot@irec.cat

[b]University of Barcelona, Barcelona 08028, Spain.

[c]Key Laboratory for Magnetism and Magnetic Materials of the Ministry of Education & School of Physical Science & Technology, Lanzhou University, Lanzhou, 730000, China.

[d]Institute for Advanced Study, Chengdu University, Chengdu, 610106, China

[e]Catalan Institute of Nanoscience and Nanotechnology (ICN2), CSIC and BIST, Campus UAB, Bellaterra, 08193, Barcelona, Spain.

[f]Catalan Institution for Research and Advanced Studies – ICREA Pg. Lluís Companys 23, 08010, Barcelona, Spain

[g]Department of Chemistry and Materials Science, Aalto University School of Chemical Engineering, P.O. Box 16100, FI-00076 Aalto, Finland.

---

*Corresponding authors.
E-mail addresses: chzhang@irec.cat (C.Y. Zhang); pmartinez@irec.cat (P. R. Martínez-Alanis), acabot@irec.cat (Andreu Cabot)

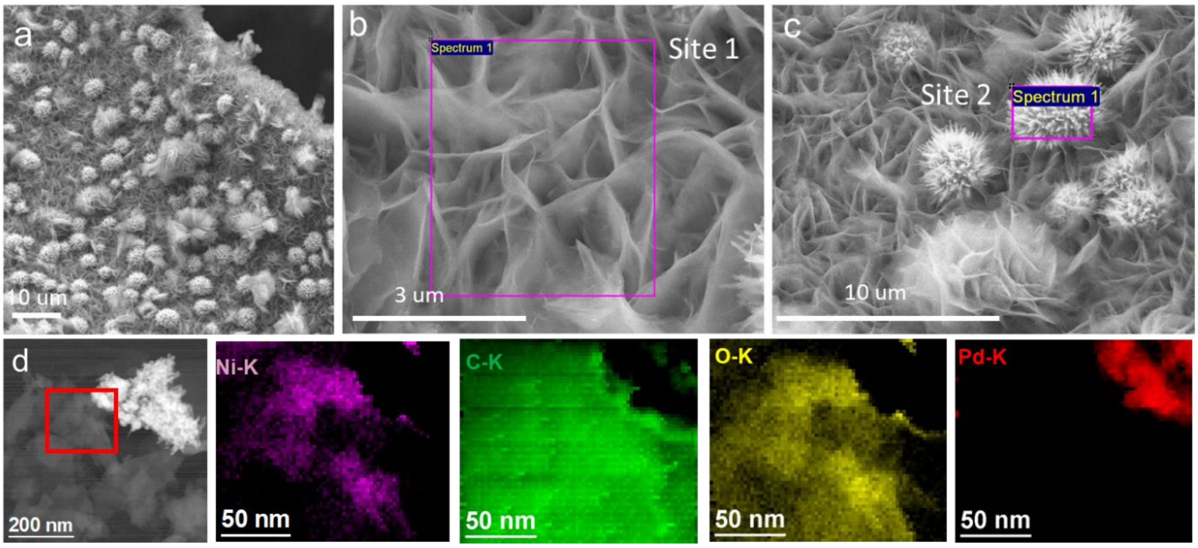

Figure S1. (a-c) SEM images of TEOA-free Pd@Ni-MOF; (d) EELS chemical composition maps obtained from the red squared area of the STEM micrograph of the sample produced without TEOA. Ni (purple), C (green), O (yellow) and Pd (red).

Table S1. EDX results of TEOA-free Pd@Ni-MOF

Element	Site 1		Site 2	
	Weight %	Atomic %	Weight %	Atomic %
C K	28	44	9.0	26
O K	40	47	20	45
Ni k	29	9.0	19	11
Pd K	2.8	0.5	52	17

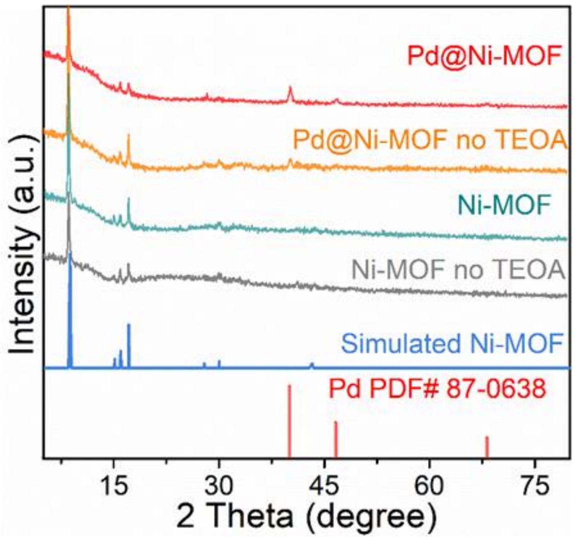

Figure S2. XRD patterns of Pd@Ni-MOF, TEOA-free Pd@Ni-MOF, TEOA-free Ni-MOF and Ni-MOF.

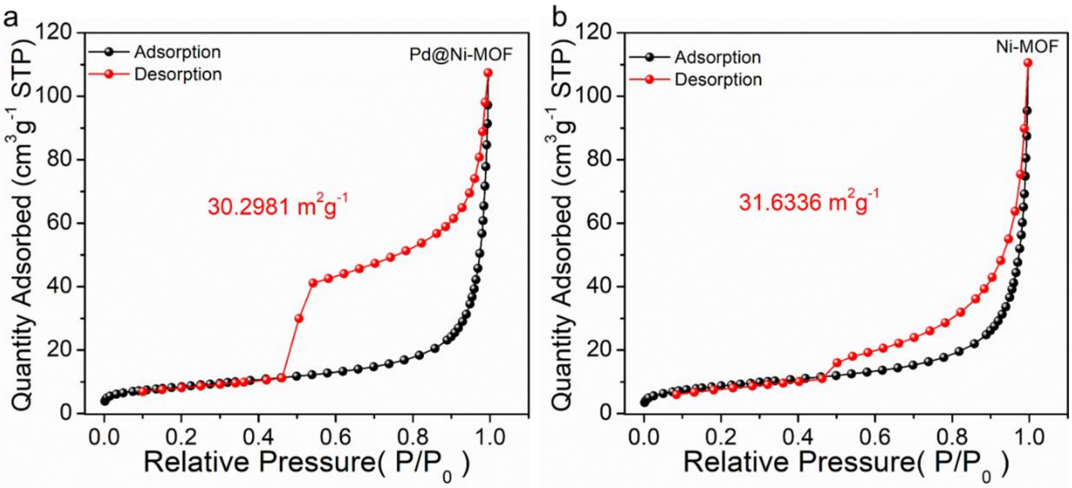

Figure S3. Nitrogen adsorption and desorption isotherms of (a) Pd@Ni-MOF and (b) Ni-MOF.

Table S2. EDX results of Pd@Ni-MOF

Element	Weight%	Atomic%
C K	31	54
O K	25	33
Ni K	29	10
Pd L	15	2.9

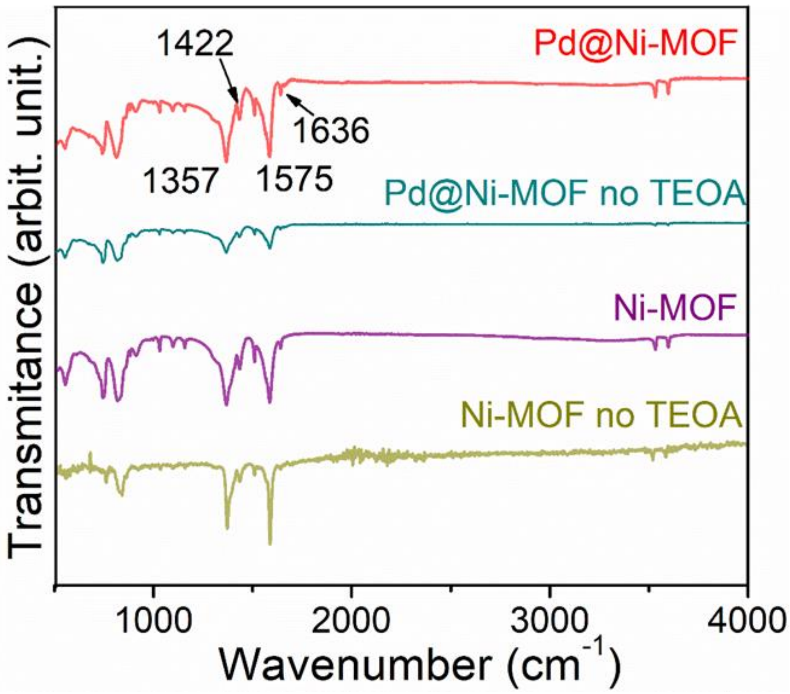

Figure S4. FT-IR spectra of Pd@Ni-MOF, TEOA-free Pd@Ni-MOF, Ni-MOF and TEOA-free Ni-MOF.

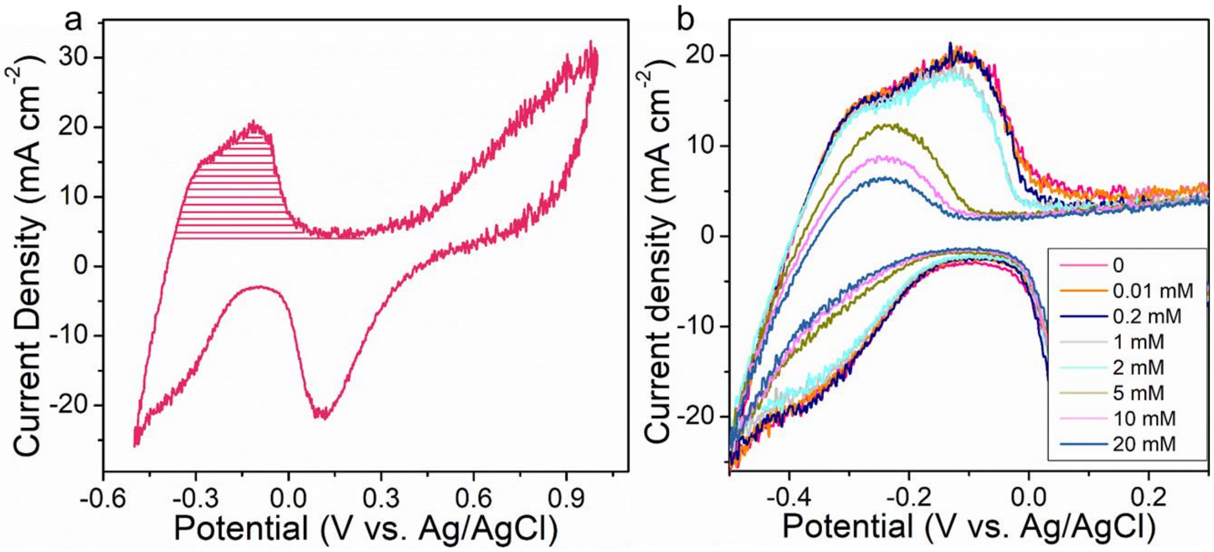

Figure S5. (a). Cyclic voltammograms measured in the presence of different concentrations of BZH (scan rate: 50 mV s^{-1}). (Reaction conditions: Sodium acetate-acetic acid (3 M) buffer (pH 5.2) electrolyte, room temperature, 1 bar N_2 flow.); (b) The shaded region was integrated to estimate the species coverage corresponding to the H_{UPD}.

Table S3. S_H integration in the absence and presence of BZH and the θ_H results of Pd@Ni-MOF, Pd@Ni-MOF(no TEOA), 20% Pd@C and Ni-MOF.

	$S_{H\ BZH\ free}$ (mA·V)	$S_{H\ BZH\ presence}$ (mA·V)	$\theta_{Hydrogen}$
Pd@Ni-MOF	18.7	7.0	0.38
Pd@Ni-MOF(no TEOA)	17.9	7.6	0.42
20% Pd@C	0.20	0.22	1
Ni-MOF	5.0	3.5	0.72

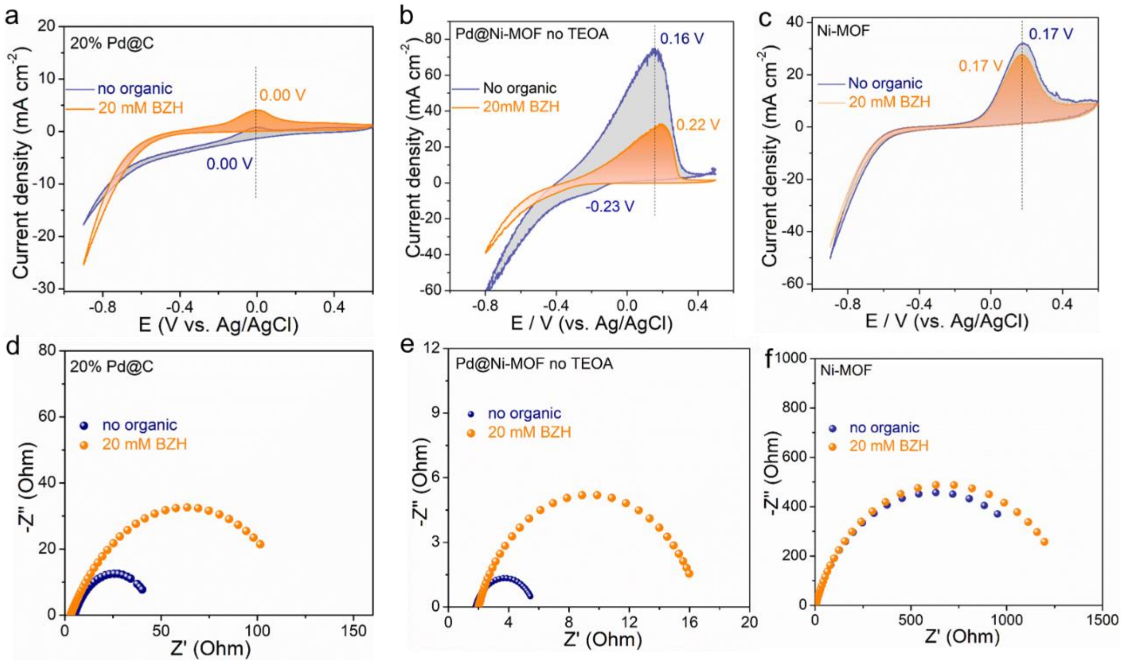

Figure S6. Cyclic voltammetry curves (a-c) and EIS (d-f) of 20% Pd@C (a,d); Pd@Ni-MOF (no TEOA) (b,e) and Ni-MOF (c,f) in the presence and absence of 20 mM BZH. Reaction conditions: Sodium acetate-acetic acid (3 M) buffer (pH 5.2) electrolyte, room temperature, 1 bar N_2 flow.

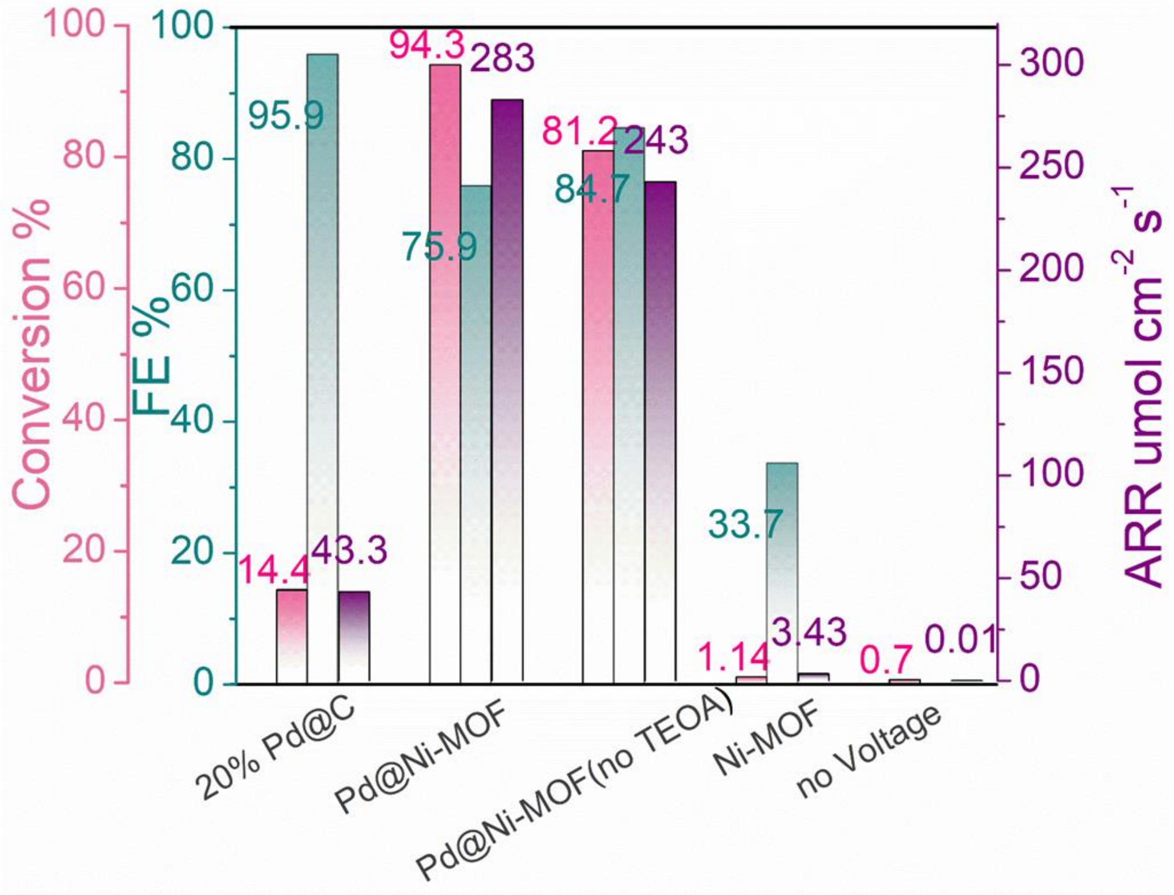

Figure S7. Comparison of the results of the electrochemical test over different materials with constant I-t (-0.6 V vs. Ag/AgCl).

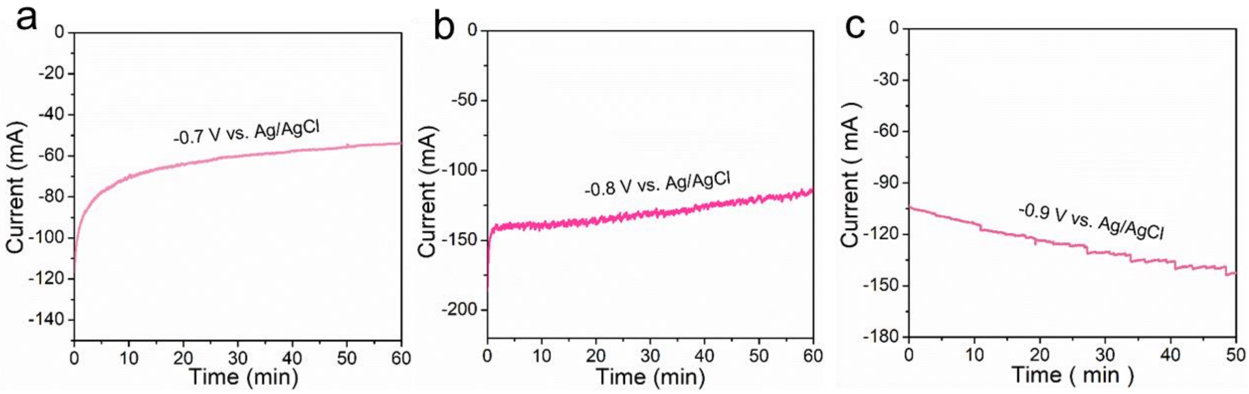

Figure S8. I-t curves at (a)-0.7 vs Ag/AgCl; (b) -0.8V vs Ag/AgCl and (c)-0.9 V vs Ag/AgCl of conversion of BZH to BA over Pd@Ni-MOF.

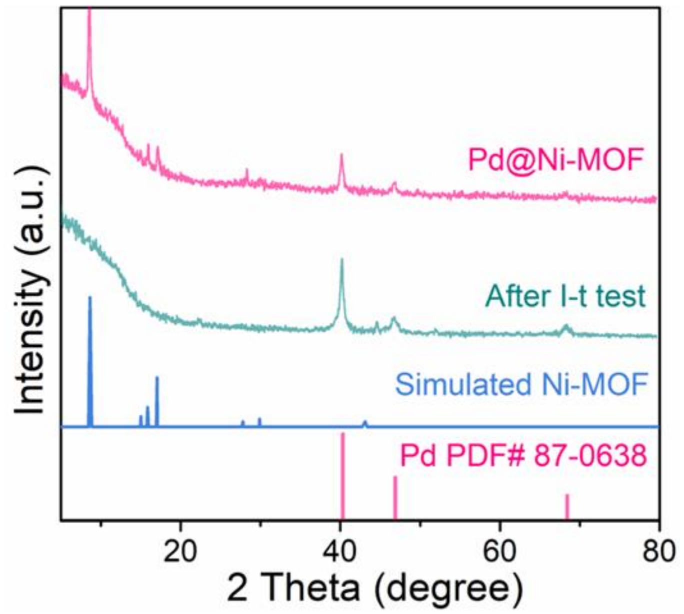

Figure S9. XRD pattern after 5 reaction cycles (60 min each).

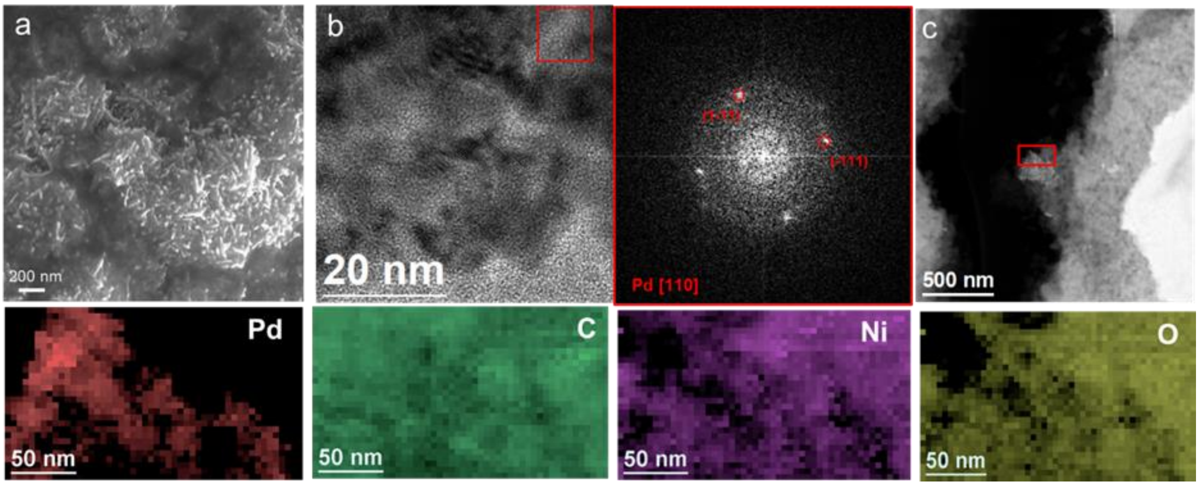

Figure S10. (a) SEM image, (b) HRTEM image and FFT analysis, (c) HAADF and EDS compositional maps of Pd@Ni-MOF after 5 reaction cycles (60 min each).

Table S4. EDX results of Pd@Ni-MOF after 5 reaction cycles (60 min each).

Element	Weight%	Atomic%
C K	13	26
O K	41	61
Ni K	13	5.4
Pd L	33	7.4

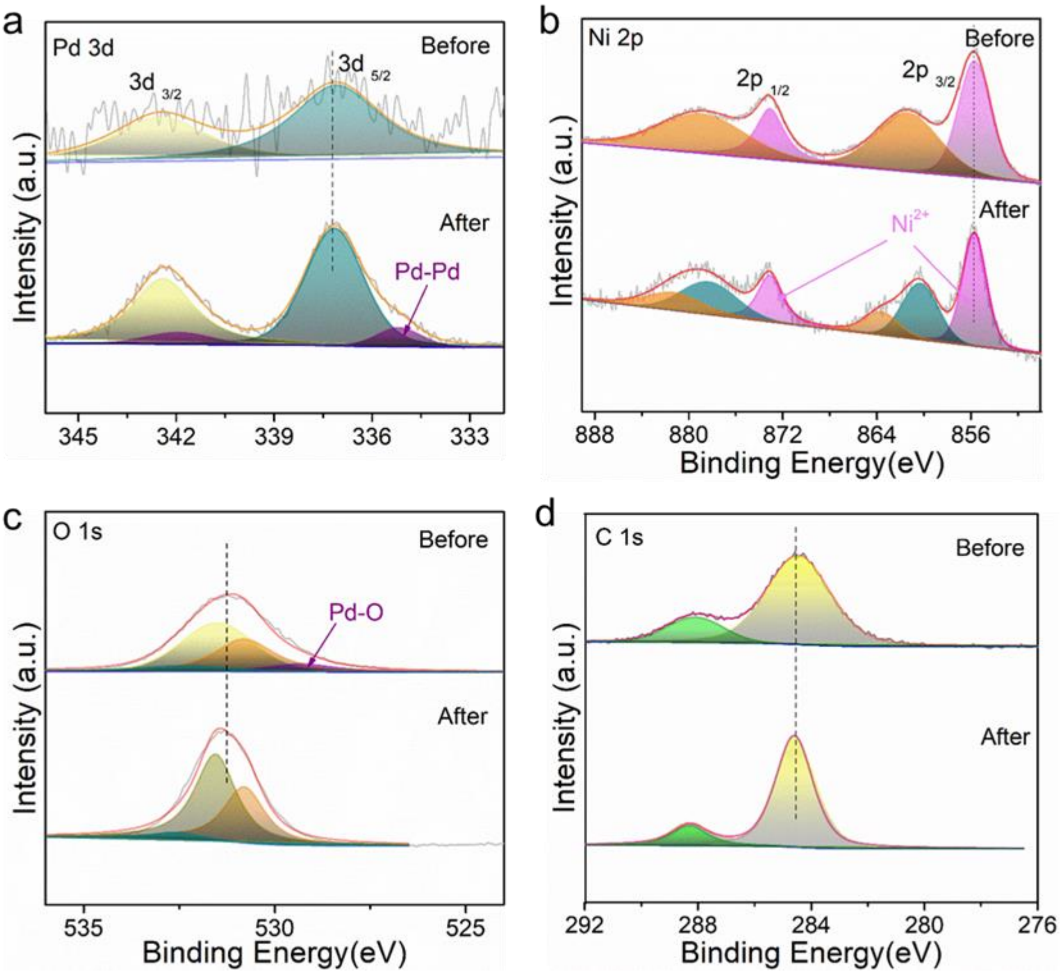

Figure S11. XPS spectra of Pd@Ni-MOF before and after 5 reaction cycles of 60 min each at the stepped voltages (a) Pd 3d; (b) Ni 2p; (c) O 1s; and (d) C 1s.

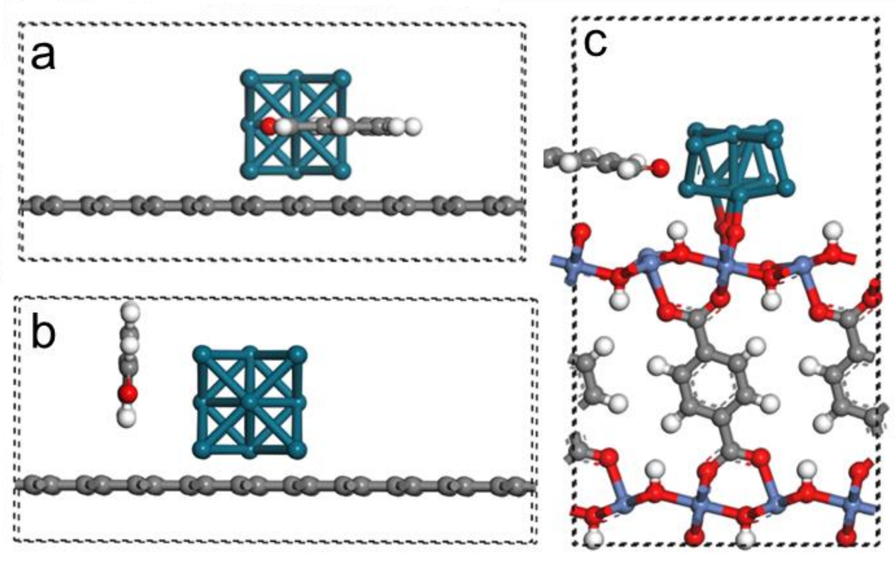

Figure S12. Schematic of adsorption configuration of BZH on (a-b) Pd@C. and (c) Pd@Ni-MOF, gray = C; green=Pd; red=O; blue=Ni.

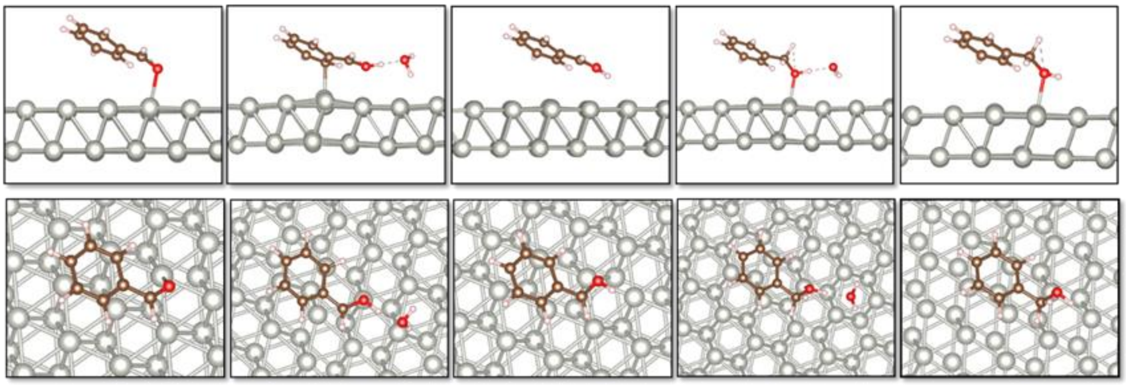

$^*CHO$ $^*CHO\text{-}H_3O^+$ $^*CHOH$ $^*CH_2O\text{-}H_3O^+$ $^*CH_2OH$

Figure S13. Structures of different species on the Pd surface

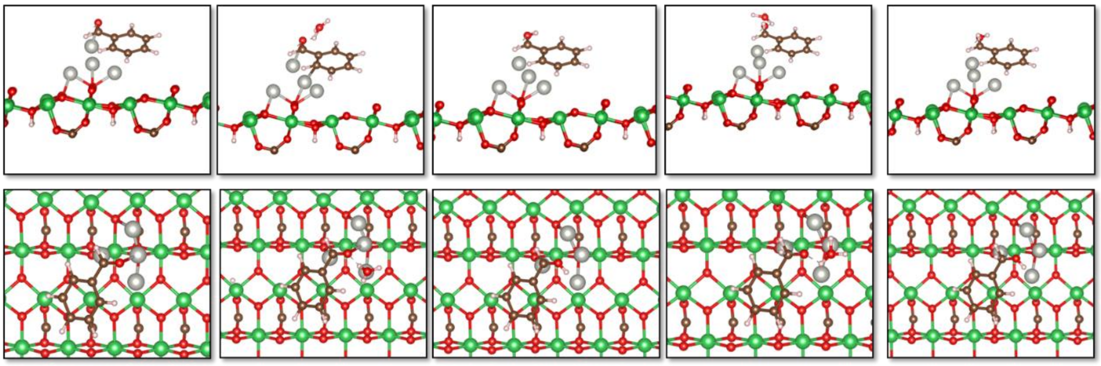

$^*CHO$ $^*CHO\text{-}H_3O^+$ $^*CHOH$ $^*CH_2O\text{-}H_3O^+$ $^*CH_2OH$

Figure S14. Structures of species on Pd@Ni-MOF surface, full model as depicted in Figure S11c.